UC Berkeley
UC Berkeley Previously Published Works

Title

Flat-band topology of magic angle graphene on a transition metal dichalcogenide

Permalink

Journal

ISSN

Authors

Wang, Tianle
Bultinck, Nick
Zaletel, Michael P

Publication Date

DOI

Peer reviewed

Flat band topology of magic angle graphene on a transition metal dichalcogenide

Tianle Wang,[1, 2] Nick Bultinck,[1, 3] and Michael P. Zaletel[1, 2]

[1]*Department of Physics, University of California, Berkeley, CA 94720, USA*
[2]*Materials Science Division, Lawrence Berkeley National Laboratory, Berkeley, California 94720, USA*
[3]*Department of Physics, Ghent university, 9000 Gent, Belgium*
(Dated: August 18, 2020)

We consider twisted bilayer graphene on a transition metal dichalcogenide substrate, where proximity-induced spin-orbit coupling significantly alters the eight flat bands which occur near the magic angle. The resulting band structure features a pair of extremely flat bands across most of the mini-Brillouin zone. Further details depend sensitively on the symmetries of the heterostructure; we find semiconducting band structures when all two-fold rotations around in-plane axis are broken, and semi-metallic band structures otherwise. We calculate the Chern numbers of the different isolated bands, and identify the parameter regimes and filling factors where valley Chern insulators and topological insulators are realized. Interestingly, we find that for realistic values of the proximity-induced terms, it is possible to realize a topological insulator protected by time-reversal symmetry by doping two holes or two electrons per superlattice unit cell into the system.

I. INTRODUCTION

Recent experimental progress [1–22] has maintained continued interest in the study of twisted bilayer graphene (TBG) in the magic angle regime, where the twist angle between the two graphene layers is approximately one degree. Near this magic angle, the TBG band spectrum structure contains eight bands near the charge neutrality point with a very small bandwidth. When the Fermi level lies within these flat bands, interactions play an important role and lead to the appearance of correlated insulating states at certain integer fillings. Interestingly, the flat bands were also found to have a subtle but non-trivial form of band topology [23–29].

In this work, we consider the band spectrum of magic angle graphene in the presence of a transition metal dichalcogenide (TMD) substrate. For some first experimental results on such TBG-TMD devices, at angles $\theta = 0.79° - 0.97°$ somewhat below the first magic angle, see Ref. [16]. The heavy atoms in a TMD substrate are known to introduce significant spin-orbit coupling (SOC) in graphene via the proximity effect. Because of their small bandwidth, the flat bands are expected to be significantly reconstructed by the SOC terms, and the band topology of the SOC bands can potentially be very different from the band topology of the original BM bands. Studying how the flat band topology changes in the presence of SOC is not purely a theoretical exercise, but is also an important step towards understanding the interacting phase diagram. One of the main reasons is that magic angle graphene has a large approximate $U(4) \times U(4)$ symmetry [30, 31], as a result of which there are many different candidate symmetry-breaking states which are very close in energy, as is seen for example in numerical Hartree-Fock [10, 30, 32, 33], density matrix renormalization group [31] and quantum Monte Carlo [34] studies. Because of this close intrinsic competition, small extrinsic effects coming from the substrate can tip the balance between different symmetry-breaking states. For example, the two-fold in-plane rotation symmetry

breaking staggered sublattice potential which is induced by an aligned hexagonal Boron-Nitride substrate has already been observed to drastically change the interacting phase diagram of magic angle graphene [11, 12, 19]. This is in agreement with the numerical Hartree-Fock study of Ref. [30], where it was found that a staggered sublattice potential as small as 10 meV can change the nature of the ground state at charge neutrality.

There are multiple different ways to combine TBG with TMD substrates, depending on whether a TMD substrate is placed on only one or on both sides of the TBG device, and depending on the in-plane orientation of the TMD relative to the graphene layers. In this work, we consider all these possibilities and find that the different devices have very different band structures. We also find that $\mathcal{C}'_{2x}$, the spinful two-fold rotation symmetry around the in-plane x-axis, plays an important role in explaining the differences in band structure. In particular, our results show that TBG-TMD heterostructures which are $\mathcal{C}'_{2x}$ symmetric have Dirac points near the Γ point, even though the spinful $\mathcal{C}_{2z}\mathcal{T}$ symmetry is broken, while C'_{2x} breaking heterostructures have a gapped band spectrum. Interestingly, we find that the gapped band structures have a pair of bands which are extremely flat around the $K^{\pm}$ point. For a representative band structure displaying this pair of flat bands, see Figs. 1(b) and 1(c), where the band structure is shown along a path between high-symmetry points in the mini-Brillouin zone. We develop an intuitive understanding of the spin-orbit coupled band structures, and in particular how they are affected by the different proximity-induced terms, by doing a $k \cdot p$ analysis at the different Dirac points.

For the devices with a gapped band spectrum, we calculate the Chern numbers of the different isolated bands. We find a very rich phase diagram depending on the relative strength of the different proximity-induced terms. We identify the parameter regions and integer filling factors where valley Chern insulators and topological insulators protected by time-reversal symmetry are realized. Interestingly, we find that for realistic values of the

proximity-induced terms, it is possible to obtain topological insulators both at filling $\nu = -2$ and $\nu = 2$, i.e. at the filling factors obtained by doping either two holes or two electrons per moiré unit cell into the system.

The remainder of this paper is organized as follows. In Section II, we start by reviewing the continuum model of twisted bilayer graphene. In Section III we consider the different TBG-TMD heterostructures, and discuss the proximity-induced terms that appear in the TBG Hamiltonian, together with their symmetries. We then first study the effect of only the leading Rashba spin-orbit coupling terms in Section IV. We use a $k \cdot p$ analysis to develop an understanding of the effects of Rashba spin-orbit coupling on the TBG flat bands, and we investigate the symmetry protection of the different Dirac cones in the bands with spin-orbit coupling. In Section V, we add the remaining subleading proximity induced terms, and analyze the resulting flat bands. Again, we resort to a $k \cdot p$ analysis to develop an intuitive understanding of the effects of the subleading terms. Next, we focus on the heterostructures which can have gapped flat bands, and we calculate the corresponding Chern numbers in Section VI. We also discuss the different topological phases that can be realized in these devices. We end with a discussion of our results in Section VII.

II. TWISTED BILAYER GRAPHENE CONTINUUM MODEL

In this section, we first review the continuum model describing twisted bilayer graphene (TBG) [35–37]. We start by defining the single-valley, spinless moiré Hamiltonian, which can be written as

$$H_K = \sum_{\mathbf{k}} H_0(\mathbf{k}) + H_T(\mathbf{k}) \,. \tag{1}$$

The first term $H_0(\mathbf{k})$ is the intra-layer term, given by

$$H_0(\mathbf{k}) = \sum_l f_l^\dagger(\mathbf{k}) h_{l\theta/2}(\mathbf{k}) f_l(\mathbf{k}) \,. \tag{2}$$

Here, $f_l^\dagger(\mathbf{k})$ denotes the electrons from layer l, each having two components from the two sublattices. $l = +/-$ is the index of top/bottom layer, and $h_\theta(\mathbf{k})$ is the monolayer graphene Hamiltonian with twist angle θ and Fermi velocity v_F:

$$h_\theta(\mathbf{k}) = \hbar v_F \left(k_x \sigma^x + k_y \sigma^y \right) e^{-i\theta\sigma^z} \,, \tag{3}$$
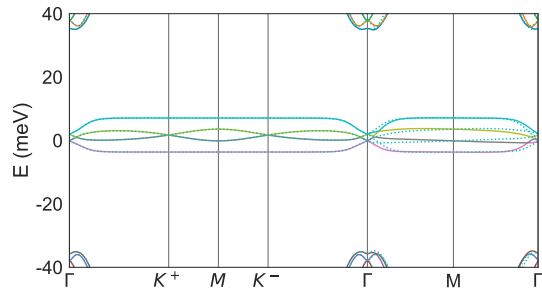
where σ acts on the electron sublattices. The top and bottom layer in $H_0(\mathbf{k})$ are rotated by $\pm\theta/2$ respectively, so the two layers have a relative twist angle θ.

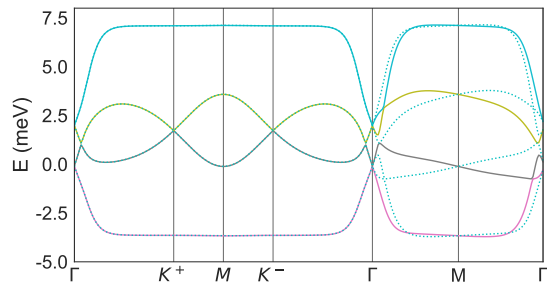The second term in Eq. (1), $H_T(\mathbf{k})$, is the inter-layer tunneling term given by

$$H_T(\mathbf{k}) = \sum_{j=1}^3 f_+^\dagger(\mathbf{k} + \mathbf{q_j}) T_j f_-(\mathbf{k}) + h.c. \,. \tag{4}$$
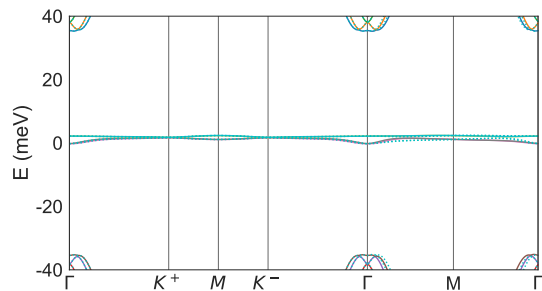
FIG. 1. (a) Band structure along a high symmetry line of the BM Hamiltonian with a Rashba SOC term given by $\lambda_R^+(\tau^z\sigma^x s^y - \sigma^y s^x)$. The twist angle is $\theta = 1.08°$, and $\lambda_R^+ = 16$ meV. (b) Same as above, but now with the Rashba SOC as $\lambda_R^- l^z(\tau^z\sigma^x s^y - \sigma^y s^x)$ which has opposite sign on both layers, and $\lambda_R^- = 16$ meV. (c) Same as (b) but zoomed in to highlight the flat bands. The solid and dotted lines represent the flat bands from different valleys.

The momentum transfer $\mathbf{q_1}$ is defined as $\mathbf{q_1} = \mathbf{K_-} - \mathbf{K_+}$, i.e. it corresponds to the momentum difference between the Dirac points of the bottom and top layer. The other two momentum transfers $\mathbf{q_2}$ and $\mathbf{q_3}$ are related to $\mathbf{q_1}$ by the three-fold rotation symmetry: $\mathbf{q_2} = \mathcal{C}_{3z}\mathbf{q_1}$, $\mathbf{q_3} = \mathcal{C}_{3z}\mathbf{q_2}$. The inter-layer hopping matrices T_j are defined as

$$T_j = w_0\sigma^0 + w_1\sigma^x e^{\frac{2\pi i}{3}(j-1)\sigma^z} \,. \tag{5}$$

The two parameters w_0, w_1 respectively correspond to the sublattice diagonal (AA/BB) and sublattice off-diagonal (AB/BA) hopping strengths respectively. In

this work, we use $w_1 = 110$ meV and $w_0 = 0.75w_1$, which takes into account corrugation effects [38–40]. For these values of the inter-layer hopping, the single-valley TBG Hamiltonian has two very flat bands around charge neutrality for twist angles close to the first magic angle value $\theta^* \sim 1.08°$.

Adding the spin and valley degrees of freedom, the complete moiré Hamiltonian for TBG takes the form

$$H_{TBG} = \begin{pmatrix} H_K(\mathbf{k}) & \\ & H_{\bar{K}}(\mathbf{k}) \end{pmatrix}_\tau \otimes s^0\,, \qquad (6)$$

where $\tau \in \{+, -\}$ labels the two valleys, and s^μ correspond to the identity matrix and the three Pauli matrices in spin space. The moiré Hamiltonians coming from different valleys are related by time reversal: $H_{\bar{K}}(\mathbf{k}) = H_K^*(-\mathbf{k})$.

The Hamiltonian H_{TBG} preserves the following symmetries: (1) Time-reversal symmetry $\mathcal{T}$; (2) $\mathcal{C}_{3z}$ rotation around the out-of-plane z-axis; (3) $\mathcal{C}_{2z}$ rotation around the z-axis and (4) $\mathcal{C}_{2x,2y}$ rotation around the in-plane x- and y-axes. For the purposes of this work, the most relevant symmetries are $\mathcal{T}$, $\mathcal{C}_{2z}$ and $\mathcal{C}_{2x}$, which respectively act as $\mathcal{T} = \tau^x \mathcal{K}$ ($\mathcal{K}$ is complex conjugation), $\mathcal{C}_{2z} = \tau^x \sigma^x$ and $\mathcal{C}_{2x} = l^x \sigma^x$. Note in particular that both $\mathcal{T}$ and C_{2z} interchange valleys, and are therefore absent in the single-valley moiré Hamiltonian $H_K(\mathbf{k})$. As expected form their geometrical definition, all two-fold rotations interchange the sublattices, and only rotations about in-plane axis interchange the two layers.

$H_0(\mathbf{k})$ contains two Dirac cones which are coupled in the presence of $H_T(\mathbf{k})$. As a result, $H_{TBG}(\mathbf{k})$ has two Dirac cones in each valley with renormalized Fermi velocity [36]. Importantly, the Dirac cones are protected by the $\mathcal{C}_{2z}\mathcal{T}$ symmetry, which acts within a single valley.

III. COMBINING TBG WITH A TMD SUBSTRATE

As is known from previous work [41], placing graphene on a transition metal dichalcogenide (TMD) substrate (such as MoS$_2$) can induce significant spin-orbit coupling (SOC) for the graphene electrons. Because the TMD lattice is highly incommensurate with graphene, its effect on the low-energy spectrum of graphene can be well approximated by a spatially-independent perturbation H_{SOC} on the graphene layer nearest to the substrate. The most important SOC terms which are induced are the Ising SOC, which takes the form

$$H_{SOC_I} = \lambda_I \tau^z s^z\,, \qquad (7)$$

and the Rashba SOC, which is given by

$$H_{SOC_R} = \lambda_R(\tau^z \sigma^x s^y - \sigma^y s^x)\,, \qquad (8)$$

where τ, σ, s act on the graphene layer proximate to the TMD. Note that magnitudes of the SOC terms in principle depend on the angle of the TMD-graphene alignment.

In particular, the TMD is not invariant under a $\mathcal{C}'_{2z}$ rotation, leading to the $\mathcal{C}'_{2z}$-odd term H_{SOC_I}: if the alignment is rotated by 180°, $\lambda_I \to -\lambda_I$. In recent experiments, the typical strengths of the different proximity-induced terms in each layer were found to be $\lambda_R \approx 16$ meV, $\lambda_I \approx 1$ meV and $u \approx 1$ meV [42–46].

In magic angle graphene the kinetic energy of the electrons is quenched and the SOC strength becomes comparable to the bandwidth of the nearly flat bands. For this reason, the SOC can potentially have a drastic effect on the moiré bands. We note that the effect of SOC on TBG was also studied previously in Ref.[16] using the same model studied here, but in the regime below the magic angle ($\theta \sim 0.8°$).

In addition to the SOC terms, the TMD also induces a finite sublattice splitting, given by

$$H_{SL} = u\sigma^z\,. \qquad (9)$$

The sublattice splitting is also induced by an aligned hexagonal Boron-Nitride substrate [47–52], and has been observed experimentally to have a non-trivial effect on the correlated phase diagram of TBG [11, 12, 19].

Because of the SOC, the TBG-TMD heterostructures is no longer invariant under the spinless symmetries mentioned in the previous section. We therefore need to consider the spinful generalizations of the three relevant symmetries discussed above, which are given by $\mathcal{T}' = i\tau^x s^y \mathcal{K}$, $\mathcal{C}'_{2z} = i\tau^x \sigma^x s^z$ and $\mathcal{C}'_{2x} = il^x \sigma^x s^x$. This will help us determine how the signs of λ_I, λ_R and u depend on the relative orientation of the TMD layer to the TBG. Namely, the $\mathcal{C}'_{2z}$ operation, which is equivalent to a 180° rotation of the TMD layer, anti-commutes with H_{SOC_I} and H_{SL} but commutes with H_{SOC_R}. This means that the λ_I and u terms will change sign upon changing the TMD orientation, but λ_R term will not. We will denote the proximity-induced terms with a $\pm$ superscript, which corresponds to their relative sign on both layers (i.e., λ_I^+ denotes Ising coupling with the same sign on both layers).

In this work, we focus on three different kinds of TBG-TMD heterostructures: (1) a TMD-TBG-TMD heterostructure with the same TMD orientation on both sides ("even"), (2) a TMD-TBG-TMD heterostructure with opposite TMD orientation on both sides ("odd"), and (3) a one-sided TBG-TMD heterostructure. The even/odd heterostructures add even/odd proximity-induced terms to the TBG Hamiltonian, respectively given by

$$H_e^{PI} = \frac{u^+}{2}\sigma^z + \frac{\lambda_I^+}{2}\tau^z s^z + \frac{\lambda_R^-}{2}l^z(\tau^z \sigma^x s^y - \sigma^y s^x)\,, \quad (10)$$

$$H_o^{PI} = l^z\left(\frac{u^-}{2}\sigma^z + \frac{\lambda_I^-}{2}\tau^z s^z + \frac{\lambda_R^-}{2}(\tau^z \sigma^x s^y - \sigma^y s^x)\right)\,. \quad (11)$$

Note that the Rashba term is required to have opposite sign on the two graphene layers by the layer-exchanging $\mathcal{C}'_{2x}$ symmetry. The one-sided TBG-TMD stacking only has proximity-induced terms on one layer, and can be

m	$(\mathcal{T},\mathcal{T}')$	$(\mathcal{C}_{2z},\mathcal{C}'_{2z})$	$(\mathcal{C}_{2x},\mathcal{C}'_{2x})$	$\mathcal{C}'_{2z}\mathcal{T}'$	$\mathcal{C}'_{2y}\mathcal{T}'$
u^+	$(\checkmark,\checkmark)$	$(\times,\times)$	$(\times,\times)$	$\times$	$\checkmark$
λ_I^+	$(\times,\checkmark)$	$(\times,\times)$	$(\checkmark,\times)$	$\times$	$\checkmark$
λ_R^+	$(\times,\checkmark)$	$(\times,\checkmark)$	$(\checkmark,\times)$	$\checkmark$	$\times$
u^-	$(\checkmark,\checkmark)$	$(\times,\times)$	$(\checkmark,\checkmark)$	$\times$	$\times$
λ_I^-	$(\times,\checkmark)$	$(\times,\times)$	$(\times,\checkmark)$	$\times$	$\times$
λ_R^-	$(\times,\checkmark)$	$(\times,\checkmark)$	$(\times,\checkmark)$	$\checkmark$	$\checkmark$

TABLE I. Symmetry transformation properties of the proximity-induced terms in Eqs. (10), (11) and (12). A "$\times$" entry in the table means that the term on that row is odd under the symmetry labeling the column, i.e. the symmetry is broken. A "$\checkmark$" entry means that the proximity-induced term is even and therefore symmetry-preserving.

written as a combination of the even and odd proximity-induced terms:

$$H_{1s}^{PI} = \frac{1+l^z}{2}\left(\frac{u}{2}\sigma^z + \frac{\lambda_I}{2}\tau^z s^z + \frac{\lambda_R}{2}(\tau^z\sigma^x s^y - \sigma^y s^x)\right). \tag{12}$$

In Table I, we list all the proximity-induced terms (Ising SOC, Rashba SOC and sublattice splitting) in both the even and odd form, and their transformation properties under time-reversal and different two-fold rotations. From the table, we see that the different TBG-TMD heterostructures are distinguished by their transformation properties under C'_{2x}. In particular, H_e breaks $\mathcal{C}'_{2x}$, while H_o is invariant under it. Importantly, because of the Ising SOC and sublattice splitting, all heterostructures necessarily break not only the spinless C_{2z} symmetry, but also the spinful C'_{2z} symmetry. All proximity-induced terms, however, do respect the spinful time-reversal symmetry $\mathcal{T}'$. As in the original TBG continuum model, the single-valley moiré Hamiltonians of the TBG-TMD heterostructures are interchanged by time-reversal symmetry.

IV. FLAT BANDS FROM RASHBA SPIN-ORBIT COUPLING

As mentioned in the last section, Rashba SOC is the dominant term introduced by the proximity effect of TMD. Therefore, we will first isolate its effect on the flat band spectrum of TBG, and later add the Ising SOC and sublattice splitting as small perturbations.

We first consider a TBG-TMD heterostructure with both even and odd Rashba SOC terms:

$$H_R = H_{TBG} + \frac{1}{2}\left(\lambda_R^+ + \lambda_R^- l^z\right)(\tau^z\sigma^x s^y - \sigma^y s^x) \tag{13}$$

H_R features four flat bands in each valley, with opposite valleys related by $\mathcal{T}'$ symmetry. In Fig. 1, we highlight the four flat bands of H_R from the K valley, with both $(\lambda_R^+, \lambda_R^-) = (16, 0)$ meV and $(\lambda_R^+, \lambda_R^-) = (0, 16)$ meV. The band spectrum with $\lambda_R^- = 0$, as shown in Fig. 1(a),

remains almost two-fold degenerate and is not very different from the original BM band spectrum. The heterostructure with $\lambda_R^+ = 0$, on the other hand, has a very intricate band structure with several remarkable features as shown in Figs. 1(b) and (c). First, near the $K^\pm$ points there is one pair of well-separated bands which are extremely flat, while the other two bands have Dirac cones at $K^\pm$. Second, we find that in total there are sixteen different linear band crossings or Dirac points, all of which are protected by the spinful $\mathcal{C}'_{2z}\mathcal{T}'$ symmetry. Two of the Dirac points are located at the Γ point, and they are displaced in energy, i.e. one Dirac point is between the top two bands and one Dirac point is between the bottom two bands. The three different $\Gamma - M$ lines each contain two linear band crossings, one between the top two bands, and one between the bottom two bands. The six final Dirac points are very close to, but not exactly on, the $\Gamma - K^+$ and $\Gamma - K^-$ lines. For the parameter values we used, we find that the Dirac points along the $\Gamma - M$ and $\Gamma - K^\pm$ are all located very closely to the Γ point. Because of the spin-orbit coupling, the two-band single-valley BM model becomes a four-band model. As a result, the chirality of the Dirac points is no longer well defined, and it is more appropriate to think about the Dirac points as carrying a non-Abelian charge [29, 53].

Below, we use a $k \cdot p$ analysis around both the $K^\pm$ and Γ points to develop an understanding of the drastically different effects of the even and odd Rashba SOC on the BM bands, and analyze the symmetry properties of the Dirac points along the $\Gamma - M$ lines.

Before diving into the details, the fundamental difference between λ_R^- [Fig. 1(b)] and λ_R^+ [Fig. 1(c)] can be summarized as follows. While far from the magic angle the two mini-Dirac points at $K^\pm$ are localized onto one-or the other layer, near the magic angle the interlayer-tunneling causes the flat bands to be delocalized 50-50 between the two layers. And as explained in more detail below, we also find the flat band states to have a relative phase difference of i between the two layers. As a result, when projecting H_R into the flat band, one finds that the effect of λ_R^+ on the two layers cancels, leaving the band structure almost unaffected, while for λ_R^- they add. The flatness of the band throughout most of the mBZ is simply a result of the momentum-independence of the Rashba coupling.

A. Analysis of the Dirac points at $K^\pm$

For our $k \cdot p$ analysis near the $K^\pm$ points, we start by considering the approximation of the "chiral limit" of tBLG, which corresponds to artificially putting $w_0 = 0$ in the BM Hamiltonian [54, 55]. In the chiral limit, the Bloch states of the flat bands around both the $K^\pm$ points can be taken to be completely localized on one of the two sublattices (i.e A vs B). Therefore, we can write the four-component Bloch states of the spinless, single-valley BM Hamiltonian in this sublattice-polarized

basis as $\psi(\mathbf{r})$ and $\chi(\mathbf{r})$, where both ψ and χ have two components corresponding to the two different layers, but live on different sublattices. The chiral Bloch states for the complete moiré Hamiltonian are then given by $\psi_{\mathbf{k}}(\mathbf{r})$, $\chi_{\mathbf{k}}(\mathbf{r})$, $\psi_{\bar{\mathbf{k}}}(\mathbf{r})$ and $\chi_{\bar{\mathbf{k}}}(\mathbf{r})$, where $\{\mathbf{k}, \bar{\mathbf{k}}\}$ denote the $K/\bar{K}$ valleys, and two spins are represented by the same Bloch states.

We can use the symmetries of the BM model to relate the different chiral Bloch states. First, H_{TBG} is invariant under $\mathcal{C}_{2z}\mathcal{T} = \sigma^x \mathcal{K}$ symmetry, which exchanges the sublattices. Therefore the Bloch states of H_{TBG} which live on different sublattices transform into each other by $\mathcal{C}_{2z}\mathcal{T}$, which implies that $\chi_{\mathbf{k}}(\mathbf{r}) = \psi_{\mathbf{k}}^*(-\mathbf{r})$. Similarly, H_{TBG} is also invariant under $\mathcal{T} = \tau^x \mathcal{K}$ symmetry, giving the following relation between other basis functions: $\{\psi_{\bar{\mathbf{k}}}(\mathbf{r}), \chi_{\bar{\mathbf{k}}}(\mathbf{r})\} = \{\psi_{-\mathbf{k}}^*(\mathbf{r}), \chi_{-\mathbf{k}}^*(\mathbf{r})\}$. These relations allow us to fix all chiral Bloch states given a single Bloch state $\psi_{\mathbf{k}}(\mathbf{r})$.

For the purpose of our $k \cdot p$ analysis, we are only interested in the chiral Bloch state $\psi_{\mathbf{k}}(\mathbf{r})$ near the $K^{\pm}$ points. We have observed numerically that in this region the chiral Bloch states are to a very good approximation given by the following simple form:

$$\psi_{K^{\pm}}(\mathbf{r}) \sim \begin{pmatrix} 1 \\ -i \end{pmatrix} f(\mathbf{r}), \tag{14}$$

where $f(\mathbf{r})$ is some envelope function which ensures that the wavefunction amplitude is concentrated on the AA regions. Eq. (14) thus implies that the wavefunction components on different layers have the same magnitude and a relative phase difference of $\pi/2$. Importantly, we find that away from the chiral limit, and even for realistic values of w_0, one can still find a basis for the flat bands where the expression in Eq. (14) remains a very good approximation for the basis states. This basis precisely corresponds to the sublattice polarized basis introduced in Ref. [30]. The observation that we can work in a basis of the form in Eq. (14) at realistic values of w_0 will help us understand many of the results obtained below.

Now we explain how we construct the $k \cdot p$ Hamiltonian near the $K^{\pm}$ points. We start with numerically diagonalizing H_{TBG} at the $K^{\pm}$ points. Because the bands at the $K^{\pm}$ are degenerate, the corresponding eigenbasis is not uniquely defined. To remedy this, we fix the eigenbasis by imposing that the $\mathcal{C}_{2z}'\mathcal{T}'$ symmetry acts as $i\sigma^x s^x \mathcal{K}$. Next, we project $H_R(\mathbf{k})$ in the neighborhood of the $K^{\pm}$ points into the symmetry-fixed eigenbasis, and obtain the following matrix:

$$\left(\tilde{H}_{R,K^{\pm}}(\mathbf{k}) \right)_{ij} \equiv \langle i | H_R(\mathbf{k}) | j \rangle , \tag{15}$$

where $|i\rangle \in \{|\psi_{K^{\pm}}\rangle, |\chi_{K^{\pm}}\rangle, |\psi_{\bar{K}^{\pm}}\rangle, |\chi_{\bar{K}^{\pm}}\rangle\}$. This procedure gives us the following effective $k \cdot p$ Hamiltonian to first order in $\mathbf{k}$:

$$\tilde{H}_{R,K^{\pm}}(\mathbf{k}) = E_{0,K} + \tilde{v}_K(k_x \sigma^x + k_y \tau^z \sigma^y) + \frac{\tilde{\lambda}_R^-}{2}(\tau^z \sigma^x s^y - \sigma^y s^x), \tag{16}$$
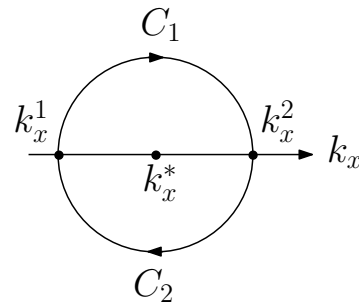

FIG. 2. $\mathcal{C}_{2x}'$ symmetric contour around a Dirac point at $\mathbf{k}^* = (k_x^*, 0)$. The contour consists of two parts C_1 and C_2, which are related by $\mathcal{C}_{2x}'$. k_x^1 and k_x^2 are the begin (end) and end (begin) points of C_1 (C_2).

where $\tilde{v}_K$ is the renormalized Dirac velocity of the tBLG. Note that under the flat band projection, the even Rashba SOC term (λ_R^+) vanishes, and therefore it has no effect on the band spectrum in first order perturbation theory. The odd Rashba terms λ_R^-, on the other hand, is unaffected by the projection. One can explicitly check these properties of the even and odd Rashba terms under projection into the flat bands by using the approximate expression for the flat band basis states given in Eq. (14).

In each valley, the projected odd Rashba SOC in Eq. (16) has eigenvalues $\{-\tilde{\lambda}_R^-, 0, 0, \tilde{\lambda}_R^-\}$. This separates two of the four zero-energy bands with quantum number $\sigma^z s^z \tau^z = -1$ with a band gap $\Delta = 2\tilde{\lambda}_R^-$, producing the flat bands in Figs. 1(b) and (c), while the other two bands remain unchanged and retain their Dirac crossing. These Dirac points are protected by the $\mathcal{C}_{2z}'\mathcal{T}'$ symmetry of H_R.

B. Analysis of the Dirac points on the $\Gamma - M$ lines

Having analyzed the Dirac cones at the K-points, we now turn our attention to those Dirac cones in the band structure of Fig. 1(c) which lie on the three different $\Gamma - M$ lines. Our goal is to identify the symmetries which protect these Dirac points. Let us first consider the Dirac cones at the Γ point, and focus on the case with $\lambda_R^+ = 0$. As a first step, we again perform a $k \cdot p$ analysis. We do this by numerically diagonalizing H_R at the Γ point, and then using the eigenstates to construct the $k \cdot p$ Hamiltonian. To fix the eigenbasis, we impose different symmetry representations with a new basis $\{\tau, \tilde{\sigma}, \tilde{s}\}$: $\tilde{\mathcal{T}}' = i\tau^y \mathcal{K}$, $\tilde{\mathcal{C}}_{2z}'\tilde{\mathcal{T}}' = \mathcal{K}$, and $\tilde{\mathcal{C}}_{2x}' = i\tau^z \tilde{\sigma}^z \tilde{s}^z$. Here, τ still refers to the valley degree of freedom, but $\tilde{\sigma}$ and $\tilde{s}$ no longer represent the original sublattices or spins, as they are now hybridized by the Rashba SOC. Instead, $\tilde{\sigma}^z$ distinguishes the pair of high energy ($\tilde{\sigma}^z = +$) and the pair of low energy bands ($\tilde{\sigma}^z = -$) at Γ, and $\tilde{s}^\mu$ acts within each pair of high or low energy bands. Note that in this basis, the $\tilde{\mathcal{C}}_{2x}'$ operator is diagonal matrix, which will be helpful for our later discussions.

After projecting $H_R(\mathbf{k})$ in the neighborhood of the Γ

point into this eigenbasis, we obtain the following effective $k \cdot p$ Hamiltonian to first order in $\mathbf{k}$:

$$\tilde{H}_{R,\Gamma} = (E_{0,\Gamma} + \tilde{m}\tilde{\sigma}^z) + \tilde{v}_\Gamma \tau^z (k_x \tilde{s}^z + k_y \tilde{\sigma}^z \tilde{s}^x) \quad (17)$$

In each valley, H_R has two separated Dirac cones at the Γ point. Similar to the Dirac cones in the BM band spectrum, they are protected by the valley-charge conservation symmetry and $\mathcal{C}'_{2z}\mathcal{T}'$.

From the $k \cdot p$ analysis we also observe that all valley-diagonal mass terms, i.e. the terms $\tau^{0,z}\tilde{\sigma}^{0,z}\tilde{s}^y$, not only break the $\tilde{\mathcal{C}}'_{2z}\tilde{\mathcal{T}}'$ symmetry, but also the $\tilde{\mathcal{C}}'_{2x}$ symmetry. As a next step, we will show that this is no accident, and that the Dirac cone at Γ is protected by the $\mathcal{C}'_{2x}$ symmetry. At the same time, we will also show that the additional Dirac points along the $\mathcal{C}'_{2x}$-invariant $\Gamma - \mathrm{M}$ line are also protected by $\mathcal{C}'_{2x}$, and that the Dirac points along the two $\Gamma - \mathrm{M}$ lines which are interchanged by $\mathcal{C}'_{2x}$ are protected by a combination of the $\mathcal{C}'_{2x}$ and $\mathcal{C}'_{3z}$ symmetries, where the latter is the spinful three-fold in-plane rotation symmetry.

To show that Dirac cones along the $\mathcal{C}'_{2x}$ invariant line are protected by $\mathcal{C}'_{2x}$, let us consider the general situation where there is a Dirac point at momentum $\mathbf{k}^* = (k_x^*, 0)$. For generality, we will also allow the $\mathcal{C}'_{2z}\mathcal{T}'$ symmetry to be broken. Denoting the cell-periodic part of the Bloch states as $|u_{\mathbf{k},n}\rangle$, the $\mathcal{C}'_{2x}$ symmetry implies that

$$D(\mathcal{C}'_{2x})|u_{\mathbf{k},n}\rangle = e^{i\alpha_n(\mathbf{k})}|u_{\mathcal{C}_{2x}\mathbf{k},n}\rangle, \quad (18)$$

where $\mathcal{C}_{2x}\mathbf{k} = (k_x, -k_y)$, $D(\mathcal{C}'_{2x})$ is the $\mathcal{C}'_{2x}$ representation acting on the periodic part of the Bloch states, and $e^{i\alpha_n(\mathbf{k})}$ is a gauge-dependent phase factor. Note that we always work in a continuous gauge, such that $\alpha_n(\mathbf{k})$ is a continuous function of momentum. Since $\mathcal{C}'^2_{2x} = -1$, the phase factors $e^{i\alpha_n(\mathbf{k})}$ satisfy $\exp(i[\alpha_n(\mathbf{k}) + \alpha_n(\mathcal{C}_{2x}\mathbf{k})]) = -1$. Along the $\mathcal{C}_{2x}$-invariant momentum line, the phase factors $\exp(i\alpha_n(\mathbf{k})) = \pm i$ are the $\mathcal{C}'_{2x}$ eigenvalues of the Bloch states. From the $\mathcal{C}'_{2x}$ transformation property in Eq. (18), it follows that the Berry connection $\mathbf{A}_n(\mathbf{k}) = i\langle u_{\mathbf{k},n}|\nabla|u_{n,\mathbf{k}}\rangle$ satisfies

$$\mathbf{A}_n(\mathbf{k}) = \mathcal{C}_{2x}\mathbf{A}_n(\mathcal{C}_{2x}\mathbf{k}) - \nabla\alpha_n(\mathbf{k}). \quad (19)$$

Note that Eq. (19) implies that the Berry curvature $F(\mathbf{k}) = \partial_x A_{n,y}(\mathbf{k}) - \partial_y A_{n,x}(\mathbf{k})$ is odd under $\mathcal{C}'_{2x}$.

Next, we consider a $\mathcal{C}_{2x}$ symmetric contour C encircling the Dirac point at $\mathbf{k}^*$. This contour consists of two parts C_1 and C_2, which are related by $\mathcal{C}_{2x}$. The two parts C_1 and C_2 meet at the points k_x^1 and k_x^2 on the $\mathcal{C}_{2x}$-invariant line $k_y = 0$. See Fig. 2 for an example of the contour C. The Berry phase along the closed contour C is given by

$$\oint_C \mathbf{A}_n(\mathbf{k}) \cdot \mathbf{dk} = \int_{C_1} \mathbf{A}_n(\mathbf{k}) \cdot \mathbf{dk} + \int_{C_2} \mathbf{A}_n(\mathbf{k}) \cdot \mathbf{dk} \quad (20)$$

Using Eq. (19), we can write the contribution to the Berry phase of the C_2 section of the contour as

$$\int_{C_2} \mathbf{A}_n(\mathbf{k}) \cdot \mathbf{dk} = -\int_{\mathcal{C}_{2x}C_1} \mathbf{A}_n(\mathbf{k}) \cdot \mathbf{dk} \quad (21)$$

$$= -\int_{C_1} \mathcal{C}_{2x}\mathbf{A}_n(\mathcal{C}_{2x}\mathbf{k}) \cdot \mathbf{dk} \quad (22)$$

$$= -\int_{C_1} (\mathbf{A}_n(\mathbf{k}) + \nabla\alpha_n(\mathbf{k})) \cdot \mathbf{dk}, (23)$$

where the minus sign in the first line comes from the fact that C_2 and $\mathcal{C}_{2x}C_1$ have different orientations, and in the third line we have used Eq. (19).

Combining Eqs. (20) and (23), we find that the Berry phase is given by

$$\oint_C \mathbf{A}_n(\mathbf{k}) \cdot \mathbf{dk} = \alpha_n(k_x^1, 0) - \alpha_n(k_x^2, 0). \quad (24)$$

Because the Berry curvature is odd under $\mathcal{C}'_{2x}$, and because the contour C is $\mathcal{C}_{2x}$ symmetric, we know that the only contribution to the Berry phase can come from the Dirac cone at $\mathbf{k}^*$. This means that the Berry phase is equal to π. From Eq. (24), it then follows that the $\mathcal{C}'_{2x}$ eigenvalues of the Bloch states along the $\mathcal{C}_{2x}$-invariant line have to change sign on crossing the Dirac point. This implies that every band has to cross an even number of Dirac points along the $\mathcal{C}_{2x}$-invariant momentum line. In a gapped band spectrum, the $\mathcal{C}'_{2x}$ eigenvalue of the Bloch states has to be constant along the $\mathcal{C}_{2x}$-invariant line $k_y = 0$, so Eq. (24) implies that the Dirac cones are protected by the $\mathcal{C}'_{2x}$ symmetry. This can also be understood by noting that since the Berry curvature is odd under $\mathcal{C}'_{2x}$, the Berry phase along any $\mathcal{C}_{2x}$-symmetric contour in a gapped band spectrum has to vanish, while this Berry phase is equal to π on encircling the Dirac point.

The arguments above show that the Dirac points along the $\mathcal{C}'_{2x}$-invariant $\Gamma - \mathrm{M}$ line are protected by the $\mathcal{C}'_{2x}$ symmetry. The $\mathcal{C}'_{3z}$ symmetry then implies that also the Dirac points along the two $\Gamma - \mathrm{M}$ lines interchanged by $\mathcal{C}'_{2x}$ cannot be gapped, which means that these Dirac crossing are protected by the combination of the $\mathcal{C}'_{2x}$ and $\mathcal{C}'_{3z}$ symmetries.

We can explicitly check the above conclusions by revisiting the $k \cdot p$ Hamiltonian in Eq. (17). The $k \cdot p$ Hamiltonian along the $k_y = 0$ line takes the form $\tilde{H}_{R,\Gamma}(k_y = 0) = E_{0,\Gamma} + \tilde{m}\tilde{\sigma}^z + \tilde{v}_\Gamma k_x \tau^z \tilde{s}^z$, and the $\mathcal{C}'_{2x}$ symmetry acts as $i\tau^z\tilde{\sigma}^z\tilde{s}^z$. From these expressions, it immediately follows that each band will indeed have opposite $\mathcal{C}'_{2x}$ eigenvalues at different sides of the Dirac points at Γ. We have also numerically computed the $\mathcal{C}'_{2x}$ eigenvalues of the four flat bands along the entire $\Gamma - M$ line, and we observed that the four bands change their $\mathcal{C}'_{2x}$ eigenvalue not only at Γ, but also on crossing the other Dirac points on the $\Gamma - M$ line. This confirms that these Dirac points are indeed protected by the $\mathcal{C}'_{2x}$ symmetry.
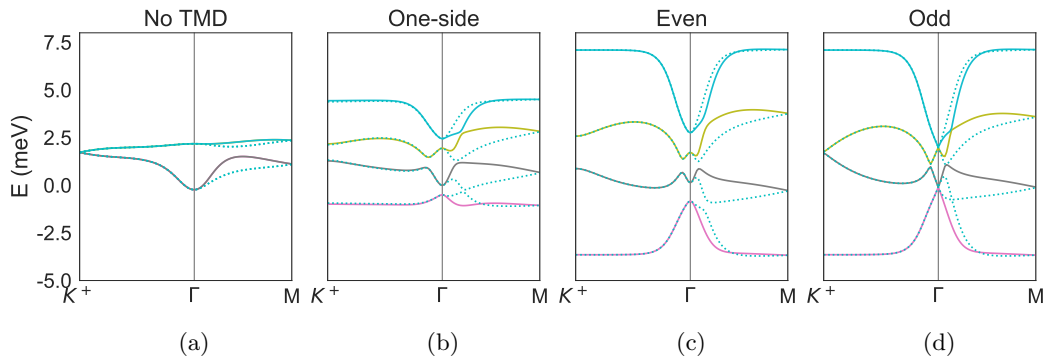
FIG. 3. Example of band spectra along $\Gamma - K^+$ line and $\Gamma - M$ line in four different kinds of devices: (a) TBG withouth TMD substrate; (b) one-sided TBG-TMD heterostructures; (c) even TMD-TBG-TMD heterostructures; (d) odd TMD-TBG-TMD heterostructures. The strengths of proximity-induced terms are $(\lambda_R, \lambda_I, u) = (16, 1, 2)$ for all figures.

V. EFFECTS OF SUBLATTICE SPLITTING AND ISING SOC

After our analysis of the effect of Rashba SOC on the BM bands, we will now include the Ising SOC and sublattice splitting terms in our analysis. Specifically, we consider the even and odd TBG-TMD heterostructure, where the Ising SOC ($\lambda_I^\pm$) and sublattice splitting ($u^\pm$) are introduced according to Eqs. (10) and (11) respectively:

$$H_{e,o} = H_{TBG} + H_{e,o}^{PI}, \qquad (25)$$

and they can be treated as perturbations to H_R in Eq. (13), with $\lambda_R^+ = 0$ and $\lambda_R^- \neq 0$. A similar treatment can be applied to one-sided TBG-TMD heterostructure

$$H_{1s} = H_{TBG} + H_{1s}^{PI}, \qquad (26)$$

but the conclusion would be similar, as we found in the previous section that the λ_R^+ term in H_{1s} has only a small effect.

Similar to Rashba SOC, the additional proximity-induced terms in H_e and H_o will change the band structure of H_{TBG}. In Fig. 3, we show the band spectra of H_e, H_o and H_{1s} along high-symmetry lines. We see that all the band spectra are gapped at the $K^\pm$ points where the gapless Dirac cones are broken by the proximity-induced terms, but the band gap in $H_{e,1s}$ are much larger than that of H_o. As for the Γ point, $H_{e,1s}$ and H_o also show different characters: H_o still retains the two gapless Dirac cones along the $\Gamma - M$ line, while $H_{e,1s}$ have all of these Dirac cones gapped out. The three Hamiltonians also gap out the Dirac cones away from high-symmetry lines, but the difference between the resulting spectra is less significant. Overall, it is expected that H_{1s} has a band spectrum similar to H_e since they share the same perturbation terms, and we will now explain the different band features of H_e and H_o in the perspective of both symmetry protection and $k \cdot p$ analysis.

We can understand the different band gaps in H_e and H_o from symmetry considerations. According to Table I,

both the $u^\pm$ and $\lambda_I^\pm$ terms in $H_{e,o}$ break the $\mathcal{C}_{2z}'\mathcal{T}'$ symmetry, removing the protection on the Dirac cones at the $K^\pm$ points. However, the u^- and λ_I^- terms in H_o preserve the $\mathcal{C}_{2x}'$ symmetry protecting the Dirac cones along the $\Gamma - M$ line, therefore they will not induce a band gap. The u^+ and λ_I^+ terms, on the other hand, do not preserve $\mathcal{C}_{2x}'$, so we do expect those Dirac cones to be gapped in H_e, but not in H_o.

The arguments above can be made explicit by using our $k \cdot p$ analysis at the $K^\pm$ and Γ points. At the $K^\pm$ points, we use the same approximate Bloch states as in the previous section to obtain a $k \cdot p$ Hamiltonian. In this way, we obtain the following effective Hamiltonians for $H_{e,o}$ near the $K^\pm$ points:

$$\tilde{H}_{e,K^\pm} = \tilde{H}_{R,K^\pm} + \tilde{u}^+ \sigma^z + \tilde{\lambda}_I^+ \tau^z s^z; \qquad (27)$$

$$\tilde{H}_{o,K^\pm} = \tilde{H}_{R,K^\pm}. \qquad (28)$$

In H_e, the additional terms in Eq. (27) gap out the Dirac cone, as they indeed break the $\mathcal{C}_{2z}'\mathcal{T}' = i\sigma^x s^x \mathcal{K}$ symmetry. Note that the $\tilde{u}^+$ and $\tilde{\lambda}_I^+$ terms commute, which implies that they are competing mass terms. As for H_o, we find that u^- and λ_I^- simply vanish under the projection involved in the $k \cdot p$ construction. This can easily be checked explicitly by using the simple approximate form for the BM Bloch states around the $K^\pm$, as discussed in detail in the previous section. Even so, u^- and λ_I^- terms still gap out the Dirac cones as these terms break the $\mathcal{C}_{2z}'\mathcal{T}'$ symmetry. The Dirac mass generated by these two terms, however, will only appear in second order perturbation theory, and will therefore be much smaller than the Dirac masses in H_e. From Fig. 3, we indeed see that the gaps at the $K^\pm$ points in H_o are significantly smaller than the corresponding gaps in H_e, which are barely visible on this scale.

At the Γ point, the $k \cdot p$ Hamiltonians corresponding to $H_{e,o}$ are

$$\tilde{H}_{e,\Gamma} = \tilde{H}_{R,\Gamma} + \tilde{u}^+ \tau^z \tilde{\sigma}^y \tilde{s}^z + \tilde{m}_I^+ \tau^z \tilde{\sigma}^z \tilde{s}^y, \qquad (29)$$

$$\tilde{H}_{o,\Gamma} = \tilde{H}_{R,\Gamma} + (\tilde{u}^- + \tilde{m}_I^-)\tau^z \tilde{\sigma}^y \tilde{s}^x, \qquad (30)$$
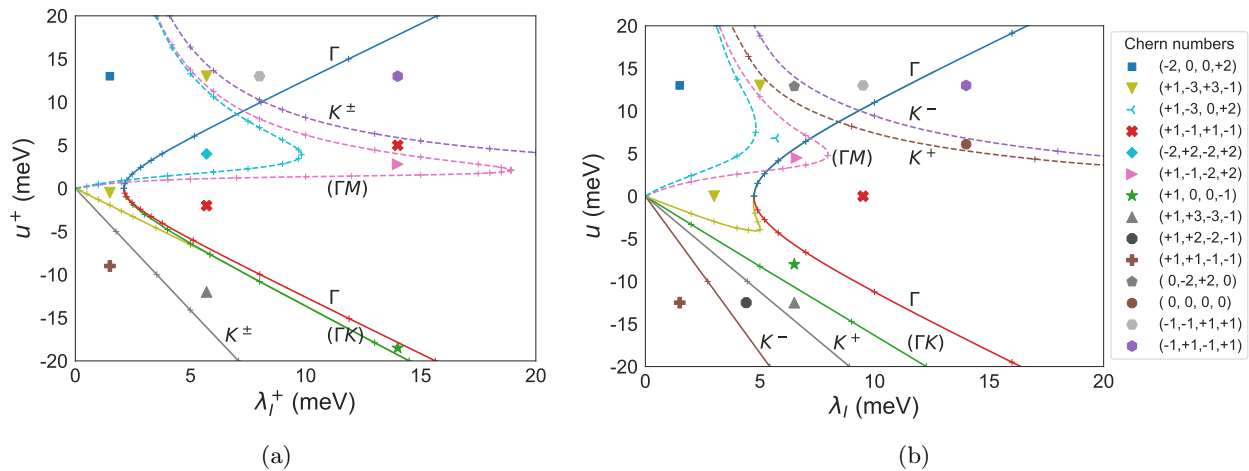
FIG. 4. Topological phases diagram of (a) even and (b) one-sided TBG-TMD heterostructures regarding (u, λ_I) parameters. Each phase is characterized by the Chern numbers of the four flat bands in K valley shown on the right. The sketched phase boundaries are where the band gap vanishes, either between the middle two bands (solid) or the top/bottom two bands (dashed), and the labels represent the position of gap closing in the momentum space.
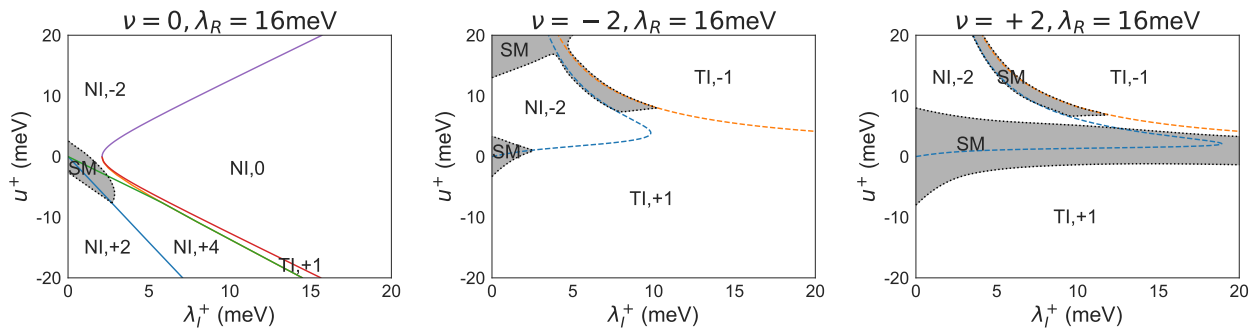

FIG. 5. The topological phase diagram of an even-aligned TBG-TMD heterostructure at $\nu = 0$, $\nu = -2$ and $\nu = +2$ filling. Each phase is labeled by the Chern number from the occupied bands in K valley, and categorized into semimetal (SM), normal insulator (NI), and topological insulator (TI) by the $\mathbb{Z}_2$ classification of TI and whether the phase is gapped or not.

With the symmetry representations $\tilde{\mathcal{C}}'_{2z} \tilde{\mathcal{T}}' = \mathcal{K}$ and $\tilde{\mathcal{C}}'_{2x} = i\tau^z \tilde{\sigma}^z \tilde{s}^z$, we see that $\tilde{H}_{e,\Gamma}$ breaks both of these symmetries, while $\tilde{H}_{o,\Gamma}$ breaks $\tilde{\mathcal{C}}'_{2z}\tilde{\mathcal{T}}'$ but not $\tilde{\mathcal{C}}'_{2x}$. This means that only H_e lifts all the symmetry protection on the Dirac cones and obtains a fully gapped bands in first order perturbation. On the other hand, H_o will only renormalize but not gap out these Dirac cones, as they are still under the protection of $\mathcal{C}'_{2x}$.

VI. VALLEY CHERN NUMBERS AND TOPOLOGICAL INSULATORS

In the previous section we found that both for the even and one-sided TBG-TMD heterostructures the flat bands can be fully gapped in the presence of all proximity-induced terms. This allows us to define Chern numbers for these isolated bands and determine their topological properties. In this section, we examine how these Chern numbers depend on the proximity-induced terms, and what topological phases can be realized in different parameter regimes and for different fillings.

We obtain the Chern numbers for the different isolated bands, as well as for different heterostructures, as follows. First, we note that since all heterostructures preserve time-reversal symmetry $\mathcal{T}'$, we only need to calculate the Chern numbers for the four flat bands in a single valley, as the bands in different valleys related by $\mathcal{T}'$ will have opposite Chern number. The Chern numbers of the isolated bands in one of the valleys are computed using the method of Ref.[56].

Since the band gaps are mainly determined by the strengths of Ising SOC λ_I and sublattice splitting u, we fix the Rashba SOC strength $\lambda_R = 16$ meV, and focus on how the Chern numbers depend on both u and λ_I. The resulting phase diagrams of the single-valley moiré Hamiltonians (in valley $\tau = +$) corresponding to both the even and one-sided heterostructures are shown in Fig. 4.

Note that it is sufficient to consider the parameter regime where $\lambda_I > 0$ because the $u^\pm$ and $\lambda_I^\pm$ change sign under $\mathcal{C}_{2z}'\mathcal{T}'$, which implies that the bands with parameters $(-u, -\lambda_I)$ have opposite Chern numbers from those with $(+u, +\lambda_I)$.

From the phase diagrams in Fig. 4, we can identify the different parameter regimes where, based on a single-particle picture, non-trivial gapped topological phases are realized in the heterostructures. In Fig. 5, we show the possible phases in the even heterostructure at fillings $\nu = -2, 0, 2$, where bands can fill in $\mathcal{T}'$-related pairs. The different topological phases are characterized by the Chern numbers of the occupied bands, and are distinguished physically in several ways. The most robust phases are those which have an odd total Chern number in each valley. These states are topological insulators which are protected by the $\mathcal{T}'$ Kramers symmetry, and are characterized by gapless helical edge modes. The phases which have an even but non-zero total Chern number in each valley are "valley-Hall" states protected only by the valley-charge conservation symmetry. In the bulk, the valley-charge conservation symmetry is preserved to a very good approximation, but it can be significantly broken along the edge of the device. Therefore, the insulators with an even but non-zero valley Chern number are separated from both the trivial and topological insulators by a bulk gap closing, even though their edge modes will acquire a small mass because of the valley-U(1) breaking terms on the edge (while we do not attempt this analysis, these phases are presumably classified by different symmetry-protected distinctions between atomic insulators). It is reasonable to expect the gap of the edge modes is smaller than the bulk gap, such that transport experiments on a device with non-zero even valley Chern number will measure a significantly smaller gap compared to devices with zero valley Chern number.

We can summarize the most relevant experimental implications of our results as follows. First, for the even and one-sided TBG-TMD heterostructure, it is possible to realize a variety of topological phases by tuning the strength of proximity-induced coupling and the filling fraction of the electron flat bands. At filling $\nu = 0$, gapped phases can be realized with valley Chern numbers $C_V = \pm 2, \pm 4$ in two-sided even heterostructures, and also $C_V = \pm 1, \pm 3$ in one-sided heterostructures. As for filling $\nu = \pm 2$, there is a large and physically realistic parameter regime where phases with $C_V = \pm 1$ can be realized, which correspond to non-trivial topological insulators protected by time-reversal symmetry.

VII. DISCUSSION AND OUTLOOK

To summarize, we have analyzed the band structures of different TBG-TMD heterostructures near the magic angle. First, the effect of the dominant Rashba SOC on the TBG flat bands was examined, and the resulting spin-orbit coupled band spectrum was found to exhibit some remarkable features such as a pair of very flat bands near the $K^\pm$ points, and a very high number of Dirac cones. Based on an approximation of the BM Bloch states near the $K^\pm$ point, we provided a simple explanation for how the Rasha SOC gives rise to the very flat bands. We also analyzed the stability of the different Dirac cones, and found that to gap out all Dirac cones one does not only need to break the spinful $\mathcal{C}_{2z}'\mathcal{T}'$ symmetry, but also the $\mathcal{C}_{2x}'$ symmetry, as the latter protects the Dirac cones on the three $\Gamma - M$ lines (as explained above, some of these Dirac cones additionally require $\mathcal{C}_{3z}'$ to be protected). Having understood the effect of the Rashba SOC, we then included the subleading Ising SOC and sublattice splitting terms. We found that $\mathcal{C}_{2x}'$ breaking heterostructures generically have a fully gapped band spectrum containing eight isolated bands, with the Ising SOC and sublattice splitting terms behaving as competing mass terms driving various phase transitions between different gapped phases. Away from the phase transitions we calculated the Chern numbers of the isolated bands, and we obtained a rich phase diagram with many topologically non-trivial phases. We explicitly identified the parameter regimes where topological insulators and valley-Hall insulators are realized at filling factors $\nu = -2, 0, 2$.

We hope that the analysis presented here can be the starting point for future experimental and theoretical work on TBG-TMD systems near the magic angle. The obvious open question is how the band structures found in this work will be affected by the Coulomb interaction. It would especially be interesting to see how the phase diagram as a function of doping at the magic angle changes in the presence of SOC, as this could potentially provide insight into the nature of the different correlated insulators and the superconducting domes. On the theoretical side, it would be interesting to apply a mean-field analysis and see if the same dominant ordering tendencies are found as in the case without SOC, and whether at the integer fillings there is perhaps a clear candidate symmetry-breaking order which has significantly lower energy. At filling factors $\nu = \pm 2$, it would be especially interesting if no sign of additional symmetry breaking is found in Hartree-Fock, and the topological insulators survive in the presence of interactions, at least on the mean-field level. We leave the study of these questions for future work.

[1] Yuan Cao, Valla Fatemi, Ahmet Demir, Shiang Fang, Spencer L. Tomarken, Jason Y. Luo, Javier D. Sanchez-Yamagishi, Kenji Watanabe, Takashi Taniguchi, Efthimios Kaxiras, Ray C. Ashoori, and Pablo Jarillo-Herrero, "Correlated insulator behaviour at half-filling in magic-angle graphene superlattices," Nature **556**, 80 EP – (2018).

[2] Yuan Cao, Valla Fatemi, Shiang Fang, Kenji Watanabe, Takashi Taniguchi, Efthimios Kaxiras, and Pablo Jarillo-Herrero, "Unconventional superconductivity in magic-angle graphene superlattices," Nature **556**, 43 EP – (2018).

[3] Matthew Yankowitz, Shaowen Chen, Hryhoriy Polshyn, Yuxuan Zhang, K. Watanabe, T. Taniguchi, David Graf, Andrea F. Young, and Cory R. Dean, "Tuning superconductivity in twisted bilayer graphene," Science **363**, 1059–1064 (2019).

[4] Alexander Kerelsky, Leo McGilly, Dante M. Kennes, Lede Xian, Matthew Yankowitz, Shaowen Chen, K. Watanabe, T. Taniguchi, James Hone, Cory Dean, Angel Rubio, and Abhay N. Pasupathy, "Magic Angle Spectroscopy," arXiv e-prints (2018).

[5] Yuhang Jiang, Xinyuan Lai, Kenji Watanabe, Takashi Taniguchi, Kristjan Haule, Jinhai Mao, and Eva Y. Andrei, "Charge order and broken rotational symmetry in magic-angle twisted bilayer graphene," Nature **573**, 91–95 (2019).

[6] Xiaobo Lu, Petr Stepanov, Wei Yang, Ming Xie, Mohammed Ali Aamir, Ipsita Das, Carles Urgell, Kenji Watanabe, Takashi Taniguchi, Guangyu Zhang, Adrian Bachtold, Allan H. MacDonald, and Dmitri K. Efetov, "Superconductors, orbital magnets, and correlated states in magic angle bilayer graphene," Nature **574**, 653–657 (2019).

[7] Yonglong Xie, Biao Lian, Berthold Jäck, Xiaomeng Liu, Cheng-Li Chiu, Kenji Watanabe, Takashi Taniguchi, B. Andrei Bernevig, and Ali Yazdani, "Spectroscopic signatures of many-body correlations in magic-angle twisted bilayer graphene," Nature (London) **572**, 101–105 (2019).

[8] Petr Stepanov, Ipsita Das, Xiaobo Lu, Ali Fahimniya, Kenji Watanabe, Takashi Taniguchi, Frank HL Koppens, Johannes Lischner, Leonid Levitov, and Dmitri K Efetov, "The interplay of insulating and superconducting orders in magic-angle graphene bilayers," arXiv preprint arXiv:1911.09198 (2019).

[9] Yu Saito, Jingyuan Ge, Kenji Watanabe, Takashi Taniguchi, and Andrea F. Young, "Decoupling superconductivity and correlated insulators in twisted bilayer graphene," arXiv e-prints (2019).

[10] Youngjoon Choi, Jeannette Kemmer, Yang Peng, Alex Thomson, Harpreet Arora, Robert Polski, Yiran Zhang, Hechen Ren, Jason Alicea, Gil Refael, Felix von Oppen, Kenji Watanabe, Takashi Taniguchi, and Stevan Nadj-Perge, "Electronic correlations in twisted bilayer graphene near the magic angle," Nature Physics **15**, 1174–1180 (2019).

[11] Aaron L. Sharpe, Eli J. Fox, Arthur W. Barnard, Joe Finney, Kenji Watanabe, Takashi Taniguchi, M. A. Kastner, and David Goldhaber-Gordon, "Emergent ferromagnetism near three-quarters filling in twisted bilayer graphene," Science **365**, 605–608 (2019).

[12] M. Serlin, C. L. Tschirhart, H. Polshyn, Y. Zhang, J. Zhu, K. Watanabe, T. Taniguchi, L. Balents, and A. F. Young, "Intrinsic quantized anomalous hall effect in a moiré heterostructure," Science **367**, 900–903 (2020).

[13] S. L. Tomarken, Y. Cao, A. Demir, K. Watanabe, T. Taniguchi, P. Jarillo-Herrero, and R. C. Ashoori, "Electronic compressibility of magic-angle graphene superlattices," Phys. Rev. Lett. **123**, 046601 (2019).

[14] Dillon Wong, Kevin P. Nuckolls, Myungchul Oh, Biao Lian, Yonglong Xie, Sangjun Jeon, Kenji Watanabe, Takashi Taniguchi, B. Andrei Bernevig, and Ali Yazdani, "Cascade of electronic transitions in magic-angle twisted bilayer graphene," Nature (London) **582**, 198–202 (2020).

[15] Uri Zondiner, Asaf Rozen, Daniel Rodan-Legrain, Yuan Cao, Raquel Queiroz, Takashi Taniguchi, Kenji Watanabe, Yuval Oreg, Felix von Oppen, Ady Stern, et al., "Cascade of phase transitions and dirac revivals in magic angle graphene," arXiv preprint arXiv:1912.06150 (2019).

[16] Harpreet Singh Arora, Robert Polski, Yiran Zhang, Alex Thomson, Youngjoon Choi, Hyunjin Kim, Zhong Lin, Ilham Zaky Wilson, Xiaodong Xu, Jiun-Haw Chu, Kenji Watanabe, Takashi Taniguchi, Jason Alicea, and Stevan Nadj-Perge, "Superconductivity without insulating states in twisted bilayer graphene stabilized by monolayer WSe$_2$," arXiv e-prints , arXiv:2002.03003 (2020), arXiv:2002.03003 [cond-mat.supr-con].

[17] Kevin P. Nuckolls, Myungchul Oh, Dillon Wong, Biao Lian, Kenji Watanabe, Takashi Taniguchi, B. Andrei Bernevig, and Ali Yazdani, "Strongly Correlated Chern Insulators in Magic-Angle Twisted Bilayer Graphene," arXiv e-prints , arXiv:2007.03810 (2020), arXiv:2007.03810 [cond-mat.mes-hall].

[18] Shuang Wu, Zhenyuan Zhang, K. Watanabe, T. Taniguchi, and Eva Y. Andrei, "Chern Insulators and Topological Flat-bands in Magic-angle Twisted Bilayer Graphene," arXiv e-prints , arXiv:2007.03735 (2020), arXiv:2007.03735 [cond-mat.mes-hall].

[19] C. L. Tschirhart, M. Serlin, H. Polshyn, A. Shragai, Z. Xia, J. Zhu, Y. Zhang, K. Watanabe, T. Taniguchi, M. E. Huber, and A. F. Young, "Imaging orbital ferromagnetism in a moiré Chern insulator," arXiv e-prints , arXiv:2006.08053 (2020), arXiv:2006.08053 [cond-mat.mes-hall].

[20] Xiaobo Lu, Biao Lian, Gaurav Chaudhary, Benjamin A. Piot, Giulio Romagnoli, Kenji Watanabe, Takashi Taniguchi, Martino Poggio, Allan H. MacDonald, B. Andrei Bernevig, and Dmitri K. Efetov, "Fingerprints of Fragile Topology in the Hofstadter spectrum of Twisted Bilayer Graphene Close to the Second Magic Angle," arXiv e-prints , arXiv:2006.13963 (2020), arXiv:2006.13963 [cond-mat.mes-hall].

[21] Xiaoxue Liu, Zhi Wang, K. Watanabe, T. Taniguchi, Oskar Vafek, and J. I. A. Li, "Tuning electron correlation in magic-angle twisted bilayer graphene using Coulomb screening," arXiv e-prints , arXiv:2003.11072 (2020), arXiv:2003.11072 [cond-mat.mes-hall].

[22] Yuan Cao, Daniel Rodan-Legrain, Jeong Min Park, Fanqi Noah Yuan, Kenji Watanabe, Takashi Taniguchi,

Rafael M. Fernandes, Liang Fu, and Pablo Jarillo-Herrero, "Nematicity and Competing Orders in Superconducting Magic-Angle Graphene," arXiv e-prints , arXiv:2004.04148 (2020), arXiv:2004.04148 [cond-mat.mes-hall].

[23] Hoi Chun Po, Liujun Zou, Ashvin Vishwanath, and T. Senthil, "Origin of mott insulating behavior and superconductivity in twisted bilayer graphene," Phys. Rev. X **8**, 031089 (2018).

[24] Hoi Chun Po, Liujun Zou, T. Senthil, and Ashvin Vishwanath, "Faithful tight-binding models and fragile topology of magic-angle bilayer graphene," Phys. Rev. B **99**, 195455 (2019).

[25] Liujun Zou, Hoi Chun Po, Ashvin Vishwanath, and T. Senthil, "Band structure of twisted bilayer graphene: Emergent symmetries, commensurate approximants, and wannier obstructions," Phys. Rev. B **98**, 085435 (2018).

[26] Zhida Song, Zhijun Wang, Wujun Shi, Gang Li, Chen Fang, and B. Andrei Bernevig, "All magic angles in twisted bilayer graphene are topological," Phys. Rev. Lett. **123**, 036401 (2019).

[27] Kasra Hejazi, Chunxiao Liu, Hassan Shapourian, Xiao Chen, and Leon Balents, "Multiple topological transitions in twisted bilayer graphene near the first magic angle," Phys. Rev. B **99**, 035111 (2019).

[28] Jianpeng Liu, Junwei Liu, and Xi Dai, "Pseudo landau level representation of twisted bilayer graphene: Band topology and implications on the correlated insulating phase," Phys. Rev. B **99**, 155415 (2019).

[29] Junyeong Ahn, Sungjoon Park, and Bohm-Jung Yang, "Failure of nielsen-ninomiya theorem and fragile topology in two-dimensional systems with space-time inversion symmetry: Application to twisted bilayer graphene at magic angle," Phys. Rev. X **9**, 021013 (2019).

[30] Nick Bultinck, Eslam Khalaf, Shang Liu, Shubhayu Chatterjee, Ashvin Vishwanath, and Michael P. Zaletel, "Ground State and Hidden Symmetry of Magic Angle Graphene at Even Integer Filling," arXiv e-prints , arXiv:1911.02045 (2019), arXiv:1911.02045 [cond-mat.str-el].

[31] Jian Kang and Oskar Vafek, "Non-Abelian Dirac node braiding and near-degeneracy of correlated phases at odd integer filling in magic angle twisted bilayer graphene," arXiv e-prints , arXiv:2002.10360 (2020), arXiv:2002.10360 [cond-mat.str-el].

[32] Ming Xie and A. H. MacDonald, "Nature of the correlated insulator states in twisted bilayer graphene," Phys. Rev. Lett. **124**, 097601 (2020).

[33] Tommaso Cea and Francisco Guinea, "Band structure and insulating states driven by Coulomb interaction in twisted bilayer graphene," Phys. Rev. B **102**, 045107 (2020), arXiv:2004.01577 [cond-mat.str-el].

[34] Yuan Da Liao, Jian Kang, Clara N. Breiø, Xiao Yan Xu, Han-Qing Wu, Brian M. Andersen, Rafael M. Fernand es, and Zi Yang Meng, "Correlation-induced insulating topological phases at charge neutrality in twisted bilayer graphene," arXiv e-prints , arXiv:2004.12536 (2020), arXiv:2004.12536 [cond-mat.str-el].

[35] J. M. B. Lopes dos Santos, N. M. R. Peres, and A. H. Castro Neto, "Graphene bilayer with a twist: Electronic structure," Phys. Rev. Lett. **99**, 256802 (2007).

[36] Rafi Bistritzer and Allan H. MacDonald, "Moiré bands in twisted double-layer graphene," Proceedings of the National Academy of Sciences **108**, 12233–12237 (2011), https://www.pnas.org/content/108/30/12233.full.pdf.

[37] E. Suárez Morell, J. D. Correa, P. Vargas, M. Pacheco, and Z. Barticevic, "Flat bands in slightly twisted bilayer graphene: Tight-binding calculations," Phys. Rev. B **82**, 121407 (2010).

[38] Nguyen N. T. Nam and Mikito Koshino, "Lattice relaxation and energy band modulation in twisted bilayer graphene," Phys. Rev. B **96**, 075311 (2017).

[39] Mikito Koshino, Noah F. Q. Yuan, Takashi Koretsune, Masayuki Ochi, Kazuhiko Kuroki, and Liang Fu, "Maximally localized wannier orbitals and the extended hubbard model for twisted bilayer graphene," Phys. Rev. X **8**, 031087 (2018).

[40] Shiang Fang, Stephen Carr, Miguel A. Cazalilla, and Efthimios Kaxiras, "Electronic structure theory of strained two-dimensional materials with hexagonal symmetry," Phys. Rev. B **98**, 075106 (2018).

[41] Martin Gmitra and Jaroslav Fabian, "Graphene on transition-metal dichalcogenides: A platform for proximity spin-orbit physics and optospintronics," Phys. Rev. B **92**, 155403 (2015).

[42] A. Avsar, J. Y. Tan, T. Taychatanapat, J. Balakrishnan, G. K. W. Koon, Y. Yeo, J. Lahiri, A. Carvalho, A. S. Rodin, E. C. T. O'Farrell, G. Eda, A. H. Castro Neto, and B. Özyilmaz, "Spin–orbit proximity effect in graphene," Nature Communications **5**, 4875 (2014).

[43] Zhe Wang, Dong-Keun Ki, Hua Chen, Helmuth Berger, Allan H. MacDonald, and Alberto F. Morpurgo, "Strong interface-induced spin–orbit interaction in graphene on ws2," Nature Communications **6**, 8339 (2015).

[44] Martin Gmitra, Denis Kochan, Petra Högl, and Jaroslav Fabian, "Trivial and inverted dirac bands and the emergence of quantum spin hall states in graphene on transition-metal dichalcogenides," Phys. Rev. B **93**, 155104 (2016).

[45] Bowen Yang, Min-Feng Tu, Jeongwoo Kim, Yong Wu, Hui Wang, Jason Alicea, Ruqian Wu, Marc Bockrath, and Jing Shi, "Tunable spin–orbit coupling and symmetry-protected edge states in graphene/ws$_2$," 2D Materials **3**, 031012 (2016).

[46] J. O. Island, X. Cui, C. Lewandowski, J. Y. Khoo, E. M. Spanton, H. Zhou, D. Rhodes, J. C. Hone, T. Taniguchi, K. Watanabe, L. S. Levitov, M. P. Zaletel, and A. F. Young, "Spin–orbit-driven band inversion in bilayer graphene by the van der waals proximity effect," Nature **571**, 85–89 (2019).

[47] B. Hunt, J. D. Sanchez-Yamagishi, A. F. Young, M. Yankowitz, B. J. LeRoy, K. Watanabe, T. Taniguchi, P. Moon, M. Koshino, P. Jarillo- Herrero, and R. C. Ashoori, "Massive Dirac Fermions and Hofstadter Butterfly in a van der Waals Heterostructure," Science **340**, 1427–1430 (2013), arXiv:1303.6942 [cond-mat.mes-hall].

[48] F. Amet, J. R. Williams, K. Watanabe, T. Taniguchi, and D. Goldhaber-Gordon, "Insulating Behavior at the Neutrality Point in Single-Layer Graphene," Phys. Rev. Lett. **110**, 216601 (2013), arXiv:1209.6364 [cond-mat.mes-hall].

[49] A. A. Zibrov, E. M. Spanton, H. Zhou, C. Kometter, T. Taniguchi, K. Watanabe, and A. F. Young, "Even-denominator fractional quantum Hall states at an isospin transition in monolayer graphene," Nature Physics **14**, 930–935 (2018), arXiv:1712.01968 [cond-mat.str-el].

[50] Jeil Jung, Ashley M. DaSilva, Allan H. MacDonald, and Shaffique Adam, "Origin of band gaps in graphene on

hexagonal boron nitride," Nature Communications **6**, 6308 EP – (2015).

[51] Matthew Yankowitz, Jeil Jung, Evan Laksono, Nicolas Leconte, Bheema L. Chittari, K. Watanabe, T. Taniguchi, Shaffique Adam, David Graf, and Cory R. Dean, "Dynamic band-structure tuning of graphene moiré superlattices with pressure," Nature (London) **557**, 404–408 (2018), arXiv:1707.09054 [cond-mat.mes-hall].

[52] Hakseong Kim, Nicolas Leconte, Bheema L. Chittari, Kenji Watanabe, Takashi Taniguchi, Allan H. MacDonald, Jeil Jung, and Suyong Jung, "Accurate Gap Determination in Monolayer and Bilayer Graphene/h-BN Moiré Superlattices," Nano Letters **18**, 7732–7741 (2018), arXiv:1808.06633 [cond-mat.mes-hall].

[53] QuanSheng Wu, Alexey A. Soluyanov, and Tomas Bzdusek, "Non-abelian band topology in noninteracting metals," Science **365**, 1273–1277 (2019).

[54] P. San-Jose, J. González, and F. Guinea, "Non-abelian gauge potentials in graphene bilayers," Phys. Rev. Lett. **108**, 216802 (2012).

[55] Grigory Tarnopolsky, Alex Jura Kruchkov, and Ashvin Vishwanath, "Origin of magic angles in twisted bilayer graphene," Phys. Rev. Lett. **122**, 106405 (2019).

[56] Takahiro Fukui, Yasuhiro Hatsugai, and Hiroshi Suzuki, "Chern numbers in discretized brillouin zone: Efficient method of computing (spin) hall conductances," Journal of the Physical Society of Japan **74**, 1674–1677 (2005), https://doi.org/10.1143/JPSJ.74.1674.